Transparent carbon nanotubes promote the outgrowth of enthorino-dentate projections in lesioned organ slice cultures

Niccolò P. Pampaloni[1] | **Ilaria Rago[2,3]** | **Ivo Calaresu[1]** | **Luca Cozzarini[2,4]** | **Loredana Casalis[2]** | **Andrea Goldoni[2]** | **Laura Ballerini** (iD) [1] | **Denis Scaini[1,2]**

[1]International School for Advanced Studies (SISSA), Trieste, Italy

[2]Elettra Sincrotrone Trieste, Trieste, Italy

[3]Department of Physics, University of Trieste, Trieste, Italy

[4]Department of Engineering and Architecture, University of Trieste, Trieste, Italy

Correspondence
Laura Ballerini and Denis Scaini, International School for Advanced Studies (SISSA), Trieste, Italy.
Email: laura.ballerini@sissa.it (L. B.) and dscaini@sissa.it (D. S.)

Present address
Niccolò P. Pampaloni, Leibniz-Forschungsinstitut für Molekulare Pharmakologie, Berlin, Germany

Abstract

The increasing engineering of carbon-based nanomaterials as components of neuroregenerative interfaces is motivated by their dimensional compatibility with subcellular compartments of excitable cells, such as axons and synapses. In neuroscience applications, carbon nanotubes (CNTs) have been used to improve electronic device performance by exploiting their physical properties. Besides, when manufactured to interface neuronal networks formation in vitro, CNT carpets have shown their unique ability to potentiate synaptic networks formation and function. Due to the low optical transparency of CNTs films, further developments of these materials in neural prosthesis fabrication or in implementing interfacing devices to be paired with in vivo imaging or in vitro optogenetic approaches are currently limited. In the present work, we exploit a new method to fabricate CNTs by growing them on a fused silica surface, which results in a transparent CNT-based substrate (tCNTs). We show that tCNTs favor dissociated primary neurons network formation and function, an effect comparable to the one observed for their dark counterparts. We further adopt tCNTs to support the growth of intact or lesioned entorhinal–hippocampal complex organotypic cultures (EHCs). Through immunocytochemistry and electrophysiological field potential recordings, we show here that tCNTs platforms are suitable substrates for the growth of EHCs and we unmask their ability to significantly increase the signal synchronization and fiber sprouting between the cortex and the hippocampus with respect to Controls. tCNTs transparency and ability to enhance recovery of lesioned brain cultures, make them optimal candidates to implement implantable devices in regenerative medicine and tissue engineering.

KEYWORDS
hippocampus, injured brain, nanomaterials, neural interfaces, regeneration, synaptic enhancement

1 | INTRODUCTION

In modern neuroscience, a large amount of (interdisciplinary) research is devoted to the development of novel therapeutic approaches to treat a variety of pathological conditions, ranging from neurodegenerative diseases (Perlmutter & Mink, 2006) to traumatic brain injuries (Finnie & Blumbergs, 2002; Girgis, Pace, Sweet, & Miller, 2016; Maas, Stocchetti, & Bullock, 2008) and psychiatric disorders (Perlmutter & Mink, 2006). An attractive strategy involves the development

---

Niccolò P. Pampaloni, Ilaria Rago, and Ivo Calaresu contributed equally to this study.

of assistive implantable devices, such as electrodes or interfaces, aimed at restoring the lost functions (Guggenmos et al., 2013). In the engineering of neuroprosthetic devices, nanotechnology demonstrated to play an important role (Cetin, Gumru, & Aricioglu, 2012), by enriching artificial scaffolds with controlled nano-sized features/cues, improving the interfacing stability with neuronal tissues at the cellular and subcellular level (Lee et al., 2006; Vidu et al., 2014; Wang et al., 2017), and providing a potential regenerative guidance. In this framework, electrically conductive nanomaterials such as carbon nanotubes (CNTs) (Iijima, 1991), are still promising, because of their tunable physicochemical features (O'Connell, 2006) and their ability to finely interact with neuronal cells (Cellot et al., 2011; Lovat et al., 2005) and neural tissues (Fabbro et al., 2012; Usmani et al., 2016). Because of these properties, CNT-endowed surfaces have been employed in the fabrication of diverse neural interfaces (Bareket-Keren & Hanein, 2013; Vidu et al., 2014), such as retinal implants (Eleftheriou et al., 2017) or deep brain stimulators (Vitale, Summerson, Aazhang, Kemere, & Pasquali, 2015). Intriguingly, CNTs were shown to improve axons regeneration and functional reconnection among segregated mammal spinal cord explants in vitro (Aurand et al., 2017; Fabbro et al., 2012; Usmani et al., 2016). However, their ability to trigger similar effects when challenged with other central nervous system (CNS) areas has yet to be shown. Besides, two significant factors that limit CNTs engineering in brain interfaces, namely their lack of optical transparency and their unstable adhesion to nanostructured films, need to be addressed. Until now, the opaqueness of CNT films directly grown via chemical vapor deposition (CVD) (Rago et al., 2019), hindering the passage of visible light, restrained the exploitation of such substrates in live imaging or optogenetic applications. On the other hand, the limited mechanical stability of CNTs films prepared following the drop casting procedure (Hokkanen, Lautala, Flahaut, & Ahlskog, 2017) to the supporting substrate may result in support detachment due to shear stresses induced by cell growth and motion (Nelson, 2017), muscular tissue contractility (Tscherter, Heuschkel, Renaud, & Streit, 2001), and/or culturing media replacement (Huber, Oskooei, Casadevall i Solvas, DeMello, Kaigala, 2018).

In this study, we take advantage of direct growth of a thin layer of CNTs on fused silica slides, which results in transparent substrates endowed with tightly bonded CNTs suitable for the assessment of functional reconnection in complex CNS organ explants. Through patch-clamp electrophysiology and immunocytochemistry experiments, we investigate whether the novel CNT–endowed substrates retain the ability to support the maturation and growth of dissociated neurons and glial cells from rat hippocampus and, more importantly, we evaluate their impact on the emerging circuit activity. We demonstrate that the novel CNT–endowed substrates can sustain the development of synaptic networks characterized by improved activity (Cellot et al., 2009, 2011; Lovat et al., 2005).

We further address the potential of tCNTs in supporting axons regeneration when coupled to complex CNS structures (Usmani et al., 2016), by interfacing tCNTs with entorhinal–hippocampal organotypic cultures (EHCs) containing the entorhinal cortex (EC), the perforant path, and the dentate gyrus. To investigate the regenerative potential of tCNTs platforms, we mimic a CNS lesion by transecting the perforant pathway, (Del Turco & Deller, 2007; Li, Field, Yoshioka, & Raisman, 1994; Parnavelas, Lynch, Brecha, Cotman, & Globus, 1974; Perederiy, Luikart, Schnell, & Westbrook, 2013; Li et al., 1993; Steward & Vinsant, 1983; Woodhams & Atkinson, 1996; Woodhams, Atkinson, & Raisman, 1993). To better reproduce a severe mechanical injury (Finnie & Blumbergs, 2002), we introduced a remarkable gap between the two portions of tissue: the hippocampus (H) was placed at 0.5 mm far apart from the EC. We show that tCNTs boost EHCs fiber sprouting ability, which ultimately leads to functional and anatomical reconnection of the two separated brain structures.

2 | RESULTS

2.1 | tCNTs synthesis and characterization

Transparent CNTs (tCNTs) were synthesized via catalytic chemical vapor deposition (CCVD) directly on fused silica slices. The synthesis was done taking advantage of the catalytic effect of iron nanoparticles (NPs) thermally obtained from a thin iron film deposited (without the employment of any adhesion layer) on the fused silica substrates. The thermal synthesis required just 90 s resulting in an ultra-thin layer of entangled CNTs decorating the slices. In our CCVD synthesis of CNTs, catalyst plays a crucial role since NPs result from a thermal annealing treatment of the substrates and they act as starting sites for the subsequent CNTs growth (Shah & Tali, 2016). Size and density of these NPs are strongly related to annealing treatment parameters (i.e., temperature and time) and the features of the initial catalyst layer (i.e., starting film thickness and its adhesion to the underneath substrate (Chiang & Sankarana, 2007). In the attempt to enhance CNT synthesis yield, one or even more intermediate metallic layers could be used as adhesion and/or anti-diffusion layer between the catalyst and the underneath support (Bayer et al., 2011; Michaelis et al., 2014). Moreover, it was reported that by setting the annealing treatment conditions at 720°C for 3 hr and the growth parameters at 720°C for 1 hr, it is possible to obtain long vertically aligned CNTs (LVA-CNTs) on various supports (Morassutto, Tiggelaara, Smithers, & Gardeniersa, 2016). Anyhow, we here demonstrated that, although any adhesion metal was employed and even if the growth time was limited to just 90 s, the yield, reproducibility, and density of the as-produced CNTs are comparable

with that of similar carbon nanostructures produced by using more time-consuming methods. Just the length of the resulting CNTs is limited and, consequently, the total thickness of the CNTs film covering the supporting substrate. Scanning electron microscopy (SEM) imaging was performed on CNTs mat to assess CNT dimensions, length, uniformity, and density. SEM micrographs (Figure 1a, left) showed a uniform carpet of short CNTs (star mark) covering a flat supporting surface of fused silica (hash mark) exposed scratching CNTs away with a razor blade. The enlargement of the dashed line-marked area pointed out a crumpled portion of the CNTs film (Figure 1a, center) allowing to estimate a film thickness of about 1 μm. A high-magnification image in correspondence of the star mark made visible the single CNTs constituting the carpet and their random orientation (Figure 1a, right) due to the absence of proximity effects (Zhang et al., 2006). Transmission electron microscopy (TEM) characterization was conducted on CNTs to explore their structure and crystallinity. It has been found that CNTs consist of multi-walled carbon nanotubes (MWNTs) with a variable number of walls. Specifically, Figure 1b shows an isolated MWNT with an outer diameter (OD) of less than 30 nm and inner diameter (ID) of approximately 10 nm. These measurements are consistent with 15 nanotube walls (Chiodarelli et al., 2012). In addition, TEM analysis revealed the presence of structural defects (Figure 1b, right), generally imperfections of conjugated sp^2 carbon along the tubes (i.e., breaks), sp^3 hybridized carbon atoms, Stone–Wales defects (i.e., two heptagons and two pentagons), presumably ascribable to the low synthesis temperature used (730°C) (Charlier, 2002; Lee, Park, Huh, & Lee, 2001). Interestingly, <2-μm-thick CNT films covering the fused silica do not prevent the light from passing through the sample (see the transmittance plot for samples of CNT film with different thickness shown in Figure 1c, left) resulting in (quasi) transparent CNT substrates. An increase in the synthesis time (e.g., 4 min) gives rise to almost opaque CNT films (Figure 1c, right). In this work, we used samples characterized by a CNT film thickness in the range of 0.2–2 μm, ultimately able to guarantee the needed optical transparency. The degree of structural ordering and the quality of our CCVD CNTs were evaluated by Raman spectroscopy. The two main bands typical of all graphite-like materials, including MWNTs, present in Raman spectra (Figure 1d) correspond to the G band at ~1,583 cm^{-1}. This band related to the in-plane tangential vibration of sp^2 carbon atoms resulting from the graphitic nature of CNTs and the D band at ~1,330 cm^{-1} indicating the presence of amorphous and/or low-ordered carbon structure (carbonaceous impurities with sp^3 bonding, and broken sp^2 bonds in the sidewalls (Costa, Borowiak-Palen, Kruszyńska, Bachmatiuk, & Kaleńczuk, 2008). The ratio between the D (I_D) and G (I_G) band integral intensities was usually adopted as an indicator of CNTs quality. Specifically, similar intensities of these bands (Antunes,

Lobo, Corat, & Trava-Airoldi, 2007), as in our case, suggested the presence of non-graphitic carbon in nanotubes, typical for low-temperature CVD-grown CNTs (Bulusheva et al., 2008). Together with the G band, the second-order Raman peak G' is characteristic of graphitic sp^2 materials and is located at ~2,700 cm^{-1}. The G' band, an overtone mode of the D band (Saito et al., 2003), is associated with defect density, but not as crucially as the first order mode. It was also reported that the intensity of this peak depends significantly on the metallicity of CNTs (Kim et al., 2007). Other peaks located at ~1,698 cm^{-1} and ~1,759 cm^{-1} are related to C = O bond vibration (Long, 1997; Roeges, 1997) and indicate possible partial oxidation of MWNTs. From the XPS survey spectrum of CNTs (Figure 1e) three elements can be discriminated: carbon (C1s), oxygen (O1s) and silicon (Si2s and Si2p). The atomic percentage of C and O are 87.6 at% and 10 at%, respectively. Only a small amount of Si was detected (2.4 at%). The presence of oxygen on CNTs surface is intrinsically related to our CVD procedure and, specifically, to defects originated during CNTs synthesis showing the tendency to adsorb oxygen when exposed to air. Figure 1f indicates the C1s core level for a ~8 μm thick CNT film. The most intense peaks located at 284.7 eV and 285.8 eV can be assigned to sp^2-hybridized graphitic carbon atoms located on CNTs walls and to amorphous carbon (sp^3-hybridized carbon atoms), respectively (Hofmann et al., 2009; Mattevi et al., 2008). The amorphous carbon is likely due to the CNTs synthesis process, as confirmed by the structural defects identified via TEM (Figure 1b) and Raman spectroscopy (Figure 1d). The peak at 290.8 eV corresponds to the electron energy loss peak due to π-plasmon excitations. These three peaks are characteristics of C1s core level from CNTs (Mudimela et al., 2014; Okpalugo, Papakonstantinou, Murphy, McLaughlin, & Brown, 2005). The additional small peaks at 287.15 eV and 288.4 eV were assigned to the presence of oxygen (Okpalugo et al., 2005).

2.2 | tCNTs biocompatibility: dissociated primary neurons growth and synaptic activity

CNTs carpets have been since long characterized as platforms enriched with nano-scaled topology able to support neural cultures development, and their effects on cultured hippocampal primary cells are well described (Cellot et al., 2009, 2011; Lovat et al., 2005). Anyway, being the result of a novel fabrication process, our first concern was to understand if the new tCNTs carpets were biocompatible and able to sustain the development of healthy and functional neural networks, potentiating the emerging synaptic activity in respect to Control cultures, as reported for opaque CNTs interfaces (Cellot et al., 2011; Lovat et al., 2005; Mazzatenta et al., 2007; Rago et al., 2019). To this aim, we compared cultured dissociated primary neurons from rat hippocampus interfaced
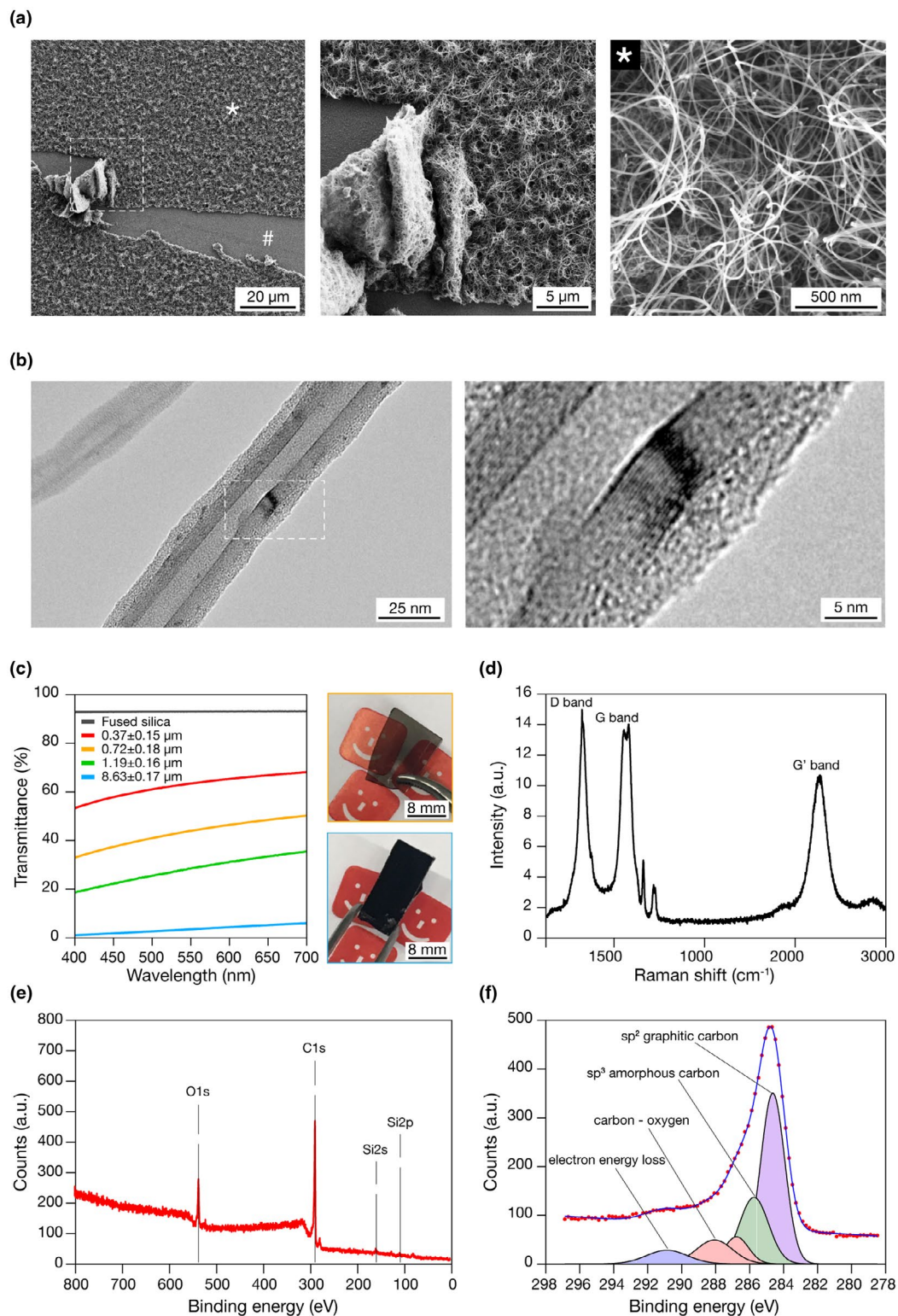
FIGURE 1 Morphological, structural, and chemical characterization of CNTs synthesized by CCVD on fused silica substrates. (a) SEM investigation of CCVD tCNT substrates reveals the uniformity of the so obtained films (left), characterized by a thickness of about 1 μm, visible in the crumpled portion of the film (center), and a random orientation of the entangled nanotubes (right). (b) TEM images of tCNTs reveals their multi-walled characteristic (left) with all the different walls constituting the tube and structural defects well visible (right). (c) Transmittance analysis in the visible spectrum of four samples characterized by different CNT film thickness compared to the pristine fused silica substrate (left); on the right, two representative optical images of a thin CNT film grown on fused silica (top, about 0.7 μm in thickness) and of a thick CNT film (bottom, about 9 μm in thickness), pointing out the good transparency of the former one. (d) Raman spectra exhibiting the characteristic D, G, and G' peaks of CVD grown MWNTs. (e) XPS survey and C1s core level (f) spectra of tCNTs grown on fused silica substrates

to tCNTs-decorated substrates with glass supported Controls. To evaluate if tCNTs were allowing the correct adhesion and growth of primary cells, we quantified the neuronal and glial cell densities after 8–10 days of in vitro growth (DIVs). Neurons and glial cells were imaged by immunofluorescence of the specific cytoskeletal components β-Tubulin III, to visualize neurons, and glial fibrillary acidic protein (GFAP)

to visualize glial cells; as shown in Figure 2a, the cellular composition of the networks developed onto Controls (left) and tCNTs (right) substrates are qualitatively comparable. We quantify the number of neurons and astrocytes composing the networks and no statistical difference in terms of cell densities were pointed out (bar plots in Figure 2b) indicating that tCNTs can sustain hippocampal cells growth in a fashion
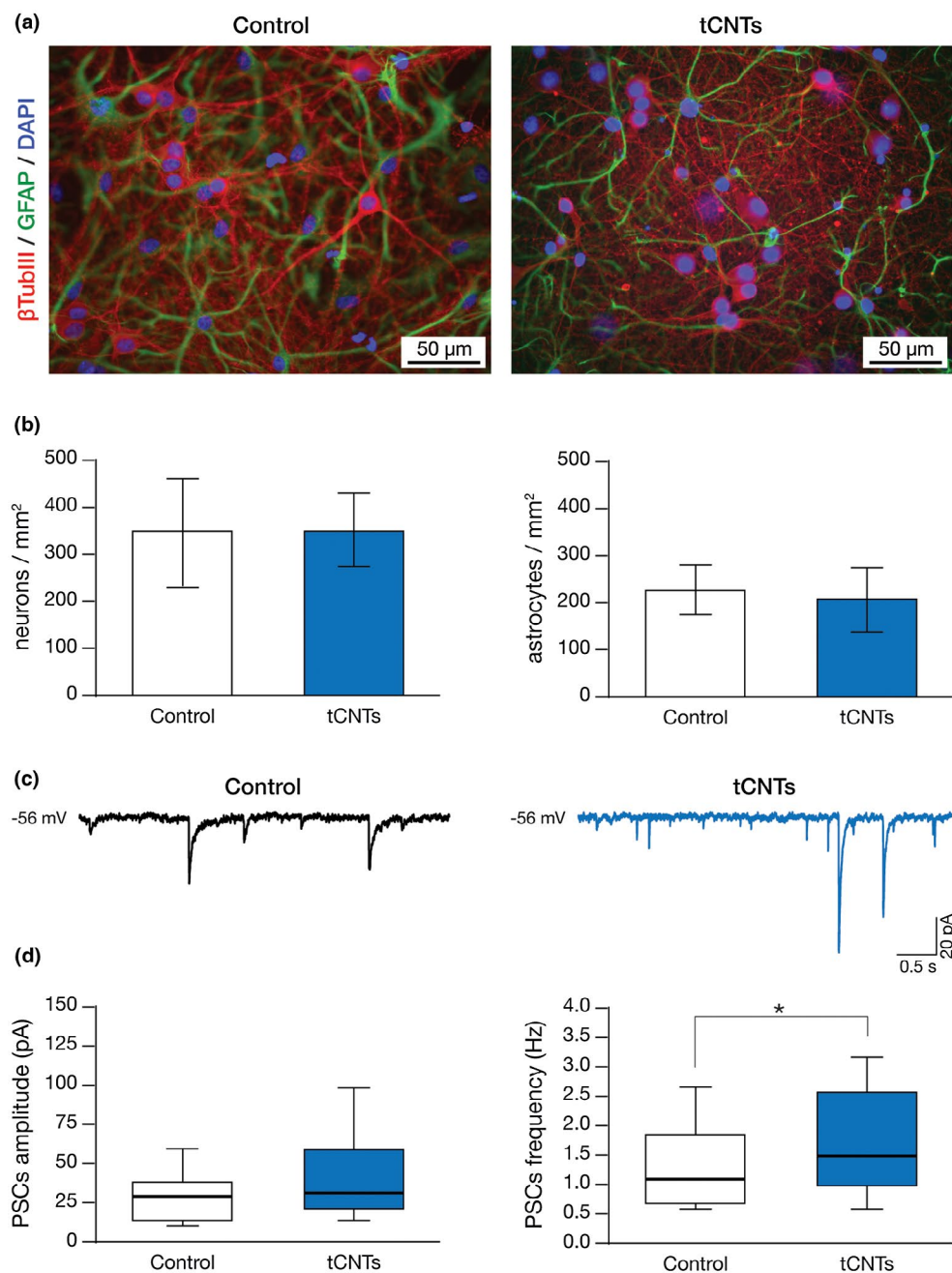

FIGURE 2 tCNTs boost the spontaneous synaptic activity of hippocampal neurons. (a) representative fluorescent micrographs depicting dissociated primary cells networks grown on glass Control substrates (left) and on tCNTs substrates (right) stained against β-Tubulin III to point out neurons (in red), GFAP to highlight astrocytes (in green) and DAPI to stain cell nuclei (in blue). (b) Bar plots summarize the density values for neuron and glia in the two growth conditions, note the absence of differences. (c) Two representative current tracings from a Control neuron (in black) and from a tCNTs neuron (in blue). (d) Box plots summarize PSCs amplitudes and frequency values. Despite no significant changes in PSCs amplitudes, a significantly higher frequency of the PSC currents related to the tCNTs condition is visible (right, $p = .03$)

similar to Control substrates. We further addressed network synaptic activity by means of single neuron, whole-cell patch clamp recordings. Figure 2c shows sample current tracings of the basal spontaneous synaptic activity of Control and tCNTs neurons, characterized by the occurrence of heterogeneous events of inward currents, displaying variable amplitudes (Mazzatenta et al., 2007). We did not detect any significant variation in the mean amplitude values of the postsynaptic currents (PSCs) in tCNT-interfaced neurons ($n = 59$ cells) when compared to Controls ($n = 40$ cells; Controls: 30 ± 2.8 pA; tCNTs 44 ± 5 pA; $p = .10$; box plots in Figure 2d, left), as well as in the membrane passive properties, such as the input resistance (Controls: 790 ± 104 MΩ; tCNTs: 587 ± 67 MΩ; $p = .10$) and membrane capacitance (Controls: 34 ± 2 pF; tCNTs: 39 ± 3 pF; $p = .20$). Conversely, we measured a significant ($p = .03$) increase in the PSCs frequencies when comparing the two conditions (Controls: 1.3 ± 0.1 Hz; tCNTs: 1.8 ± 0.1 Hz; Figure 2d, right). By these preliminary tests, we concluded that the newly manufactured tCNTs allow hippocampal cell adhesion, viability, synaptic network development and promote enhanced synaptic activity, an effect reminiscent of what reported when interfacing neurons to CNT carpets (drop casted or thick CVD growth films; Cellot et al., 2009, 2011; Lovat et al., 2005; Mazzatenta et al., 2007; Rago et al., 2019).

2.3 | Organotypic entorhinal–hippocampal cultures growth interfaced to tCNTs

In the second set of experiments, we tested tCNTs, characterized by transparency and strong adhesion to the underneath fused silica substrate, as growth interfaces for intact and injured CNS explants. In particular, we focused on the entorhinal–hippocampal system. As shown by low-magnification immunofluorescence images in Figure 3a, intact EHC successfully grew interfaced to tCNTs, in a way similar to Controls EHCs (Figure 3a, right and left, respectively). To challenge the regenerative potential of the new tCNTs, we simulated a severe mechanical lesion at the subicular level by surgical complete transection. After transecting the tissue, the EC and hippocampus (H) components where cultured (8–12 DIV) at a distance of 500 ± 100 μm apart (Figure 3b; see Methods). Also after denervation, we detected adhesion, survival, and growth of the organotypic cultures on both tCNTs and Control (Figure 3b, right and left, respectively). We adopted this configuration to reproduce in vitro a traumatic event due to mechanical injury, resulting in anatomical and functional disconnection of the two brain regions. A severe perforant pathway (PP) transection at the subicular level is a widely exploited and generally accepted model to investigate neural circuits plasticity in response to brain injury, adopted in vivo and in organotypic slices (Perederiy & Westbrook, 2013; Vlachos et al., 2012; Vuksic et al., 2011).

We next investigated the functional impairments following the lesion and the residual neuronal activity in both the EC and H slices (Perederiy & Westbrook, 2013).

2.4 | tCNTs enhance the entorhinal–hippocampal field potential synchronization

We performed simultaneous local field potential (LFP) recordings by placing one electrode in the H within the molecular layer of the dentate gyrus (DG), and a second one within the deep layer (IV/V) of the EC. LFPs are voltage signals that reflect collective multiple neurons membrane activities. We compared the spontaneous basal activities emerging upon 8–12 DIV between intact EHC and the lesioned one, in which the PP was totally resected and the two (emi)-portions of the EHC displaced (see the cartoon in Figure 3c). Field recordings were performed in standard saline solution (see Methods) for intact and lesioned EHCs developed on glass substrates (sketched in Figure 4a; $n = 7$ and $n = 9$, respectively) or interfaced with tCNTs (sketched in Figure 4b; $n = 5$ and $n = 6$, respectively).

We quantified DG spontaneous activity when grown on Control glass substrates, by measuring the LFPs inter-event intervals (IEIs). Upon prolonged denervation, IEIs show a significant (cumulative distribution in Figure 4c, top plot for DG; $p < .001$) increase in duration in lesioned EHCs when compared to the intact slices, testifying a reduction in DG excitation. Similarly, LFPs in EC on Control substrates showed a significant increase in IEIs duration in lesioned EHCs when compared to the intact slices (cumulative distribution in Figure 4c, bottom plot; $p < .001$). Thus, in Control conditions, denervation usually determined a reduction in the occurrence of LFPs. When analyzing EHCs interfaced to tCNTs, in the intact organ slices we detected higher LFPs occurrence in DG when compared to glass Controls (cumulative distribution in Figure 4c, top plot; $p < .001$). To note, in DG, LFPs activity was further enhanced after 8–12 DIV of denervation, even when compared to intact tCNTs cultures (i.e., lower IEI values; cumulative distribution in Figure 4c, top plot; $p < .01$). A similar behavior was observed when measuring the distribution of IEIs values of LFPs recorded from the EC interfaced to tCNTs, in intact or injured EHC (cumulative distribution in Figure 4c, bottom plot; $p < .001$). These results suggest that in intact slices, tCNTs interfacing promote an increase in spontaneous activity, reminiscent of the material effect detected in spinal slice cultures (Fabbro et al., 2012), and presumably due to the reported ability of CNT-based interfaces to enhance synaptic networks (Cellot et al., 2011; Fabbro et al., 2012; Lovat et al., 2005; Mazzatenta et al., 2007).

Regardless of the intact EHCs, in lesion ones tCNTs interfacing has the ability to promote LFP occurrence in both DG and EC slices when compared to injured glass Controls
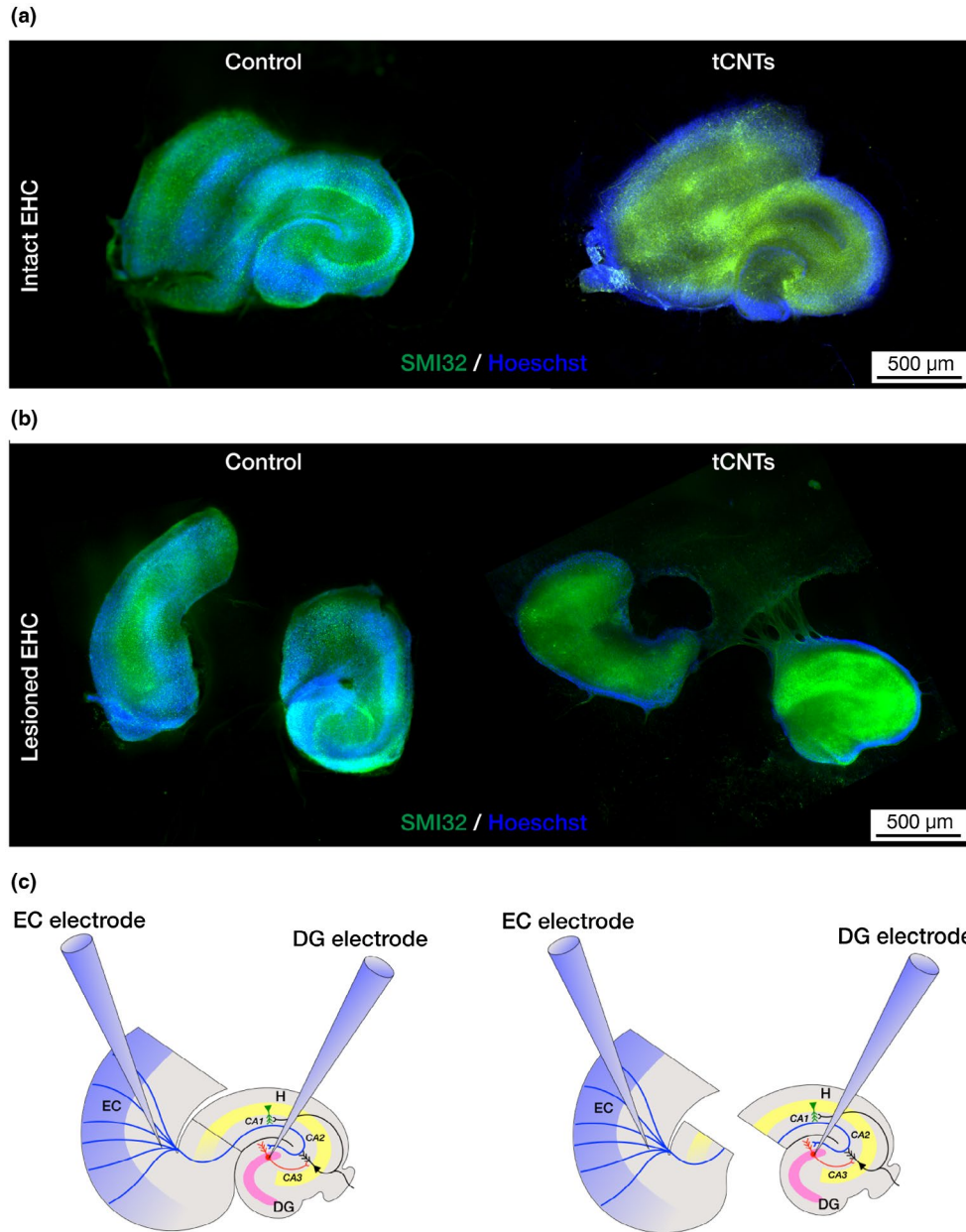
FIGURE 3 tCNTs are suitable substrates for the development of healthy EHCs organotypic cultures. (a) Representative epifluorescence stitched images showing 8-day-old organotypic EHCs cultures stained with Hoetsch to make visible all cell nuclei (blue) and NeuN to highlight just neuronal nuclei (green) in the intact organotypic slice when cultured on glass Control (left) and tCNTs (right). (b) Representative images of 8-day-old lesioned EHCs organotypic cultures stained with Hoetsch (blue) and NeuN (green) and cultured on glass Control (left) and tCNTs (right). Both intact and lesioned EHC organotypic cultures displayed a similar morphology when grown on Control and tCNTs substrates. (c) Representative sketch depicting the experimental setup: entorhinal cortex (EC), the dentate gyrus (DG) in the hippocampus (H) and a clear vision of the perforant pathway (blue path) together with the Shaffer collaterals (black path) and mossy fiber pathway (red path). Field potential extracellular recordings were simultaneously performed from the EC (left electrode) and the hippocampal DG (right electrode) in the intact (left) and injured (right) EHC slice

(Figure 4d, blue and red box plots, respectively; Control: $n = 9$, tCNT: $n = 6$; $p < .001$), a result that might indicate the ability of tCNTs in promoting functional changes in excitatory synapses post-denervation, alternatively tCNTs might also favor regeneration and synaptic targeting of the injured PP axons (Usmani et al., 2016).

To assess whether tCNTs have the ability to promote PP regeneration and synaptic targeting, we assessed the functional connectivity between the DG and the EC in intact and lesion EHC when interfaced to the two different substrates by cross-correlation analysis of the simultaneously recorded, spontaneous LFPs. Interestingly, in intact EHC,
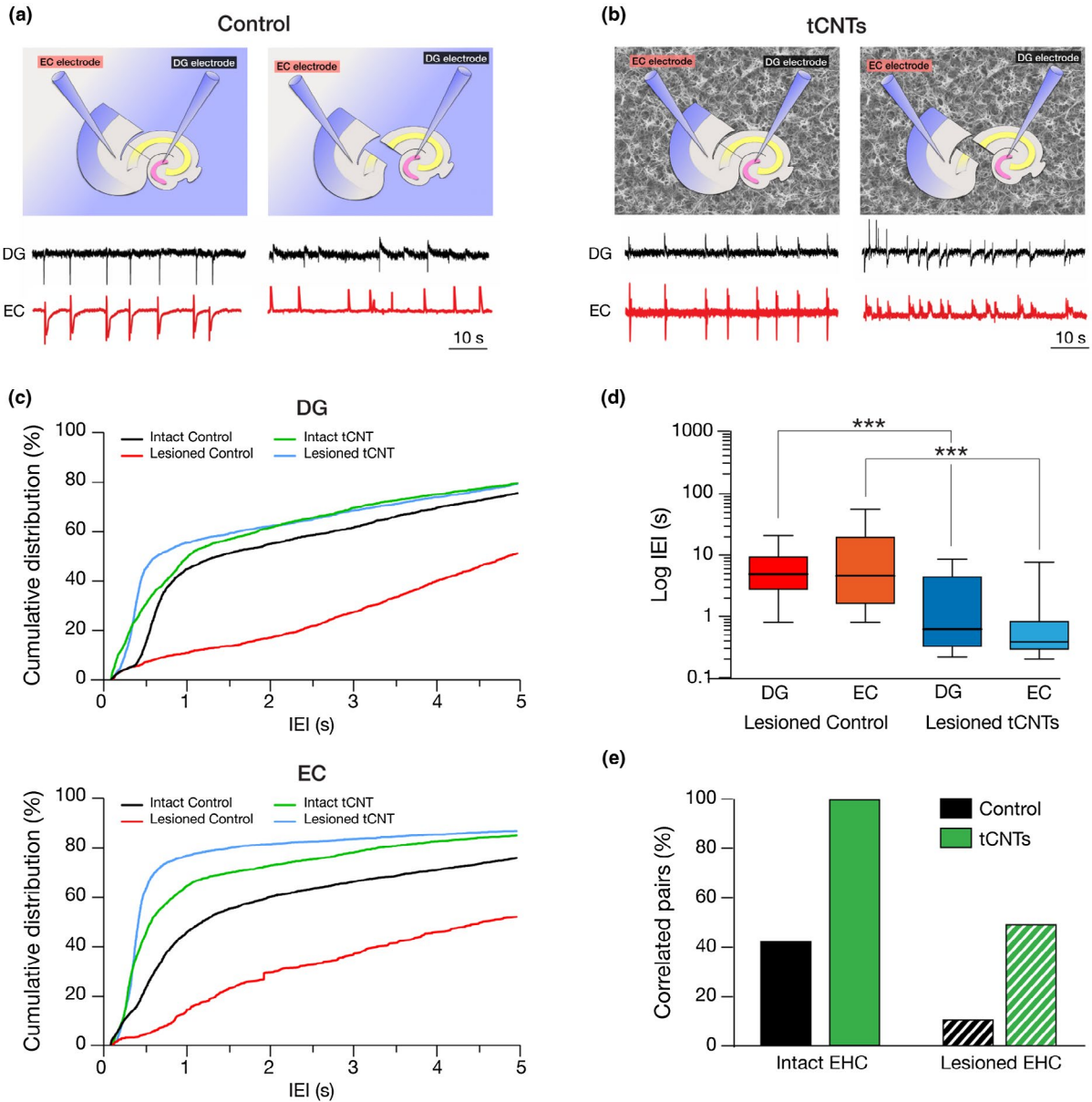
FIGURE 4 tCNTs enhance the EC–DG signal synchronization in EHCs. (a) A sketch of the intact EHC (left) and the lesioned one (right) when cultured on glass slide Controls. Below, two representative voltage traces for the DG (black trace) and EC (red trace) are shown in standard saline solution. (b) A similar sketch of the intact EHC (left) and the lesioned one (right) when interfaced to tCNTs. Below, two representative voltage traces for the DG (black trace) and EC (red trace) are shown in standard saline solution. (c) The cumulative distribution function of IEIs up to 5 s is shown for DG (top) and EC (bottom). When interfaced to tCNTs, the activity of both DG and EC is accelerated, as appreciable from the IEIs cumulative distributions (green and blue lines), characterized by a significantly larger population of brief IEI when compared to glass Controls (black and red lines). (d) Box plots of IEI values for the lesioned EHC shown in logarithmic scale for Controls and tCNTs, note the significant drop in IEIs duration in tCNTs-interfaced tissues. (e) Bar plots summarize the correlated DG and H pair recordings in intact and injured EHCs, both in Control and tCNT substrates

only 43% of Controls DG and EC displayed a Pearson's correlation coefficient (CCF) that was significantly larger than that expected by chance (see Methods; Usmani et al., 2016), such a value was increased to 100% in intact tCNT recordings (summarized by bar plot in Figure 4e). In lesioned EHCs, correlated LFPs dropped to 11% of Controls, while 50% of tCNTs LFPs recordings were still correlated

(bar plot in Figure 4e). Thus, injured EHC, upon 8–12 DIV interfaced to tCNTs, displayed a lower impairment in spontaneous LFPs characterized by a larger connectivity, as supported by the higher synchronization of the two segregated EHC portions. These results suggest that tCNTs enhanced the regeneration of PP fibers and promote synaptic targeting when interfacing lesioned EHC.

2.5 | tCNTs favor regrowth of active fibers in injured EHC slices

To assess whether tCNTs promoted new fibers sprouting leading to a more functional bridge between the EC and H sections, we tested the ability of stimulating EC superficial layers, where the PP is known to originate (Jacobson & Marcus, 2008; Witter, 2007; Witter & Amaral, 2004) in evoking LFPs in injured EHC. The two recording electrodes were positioned in the same configuration used for simultaneous recordings of DG and EC spontaneous LFPs, while an additional stimulating electrode was placed in the superficial

layers of the EC (see sketches in Figure 5a, left). We, therefore, proceeded with the PP stimulation (see Methods), and we grouped the evoked LFPs into three categories: the first, when the stimulation evoked successful responses from both EC and DG; the second, when the response was evoked only in the EC; or, third, only in the DG. Tracings in Figure 5a, right panel, shows sample voltage tracings depicting these three responses (in blue, green, and magenta, respectively), for the lesioned EHC.

In intact ECHs, regardless the presence of tCNTs, PP stimuli always evoked LFPs in both EC and DG (Figure 5b, top; Control: $n = 4$; tCNTs: $n = 4$). On the opposite,
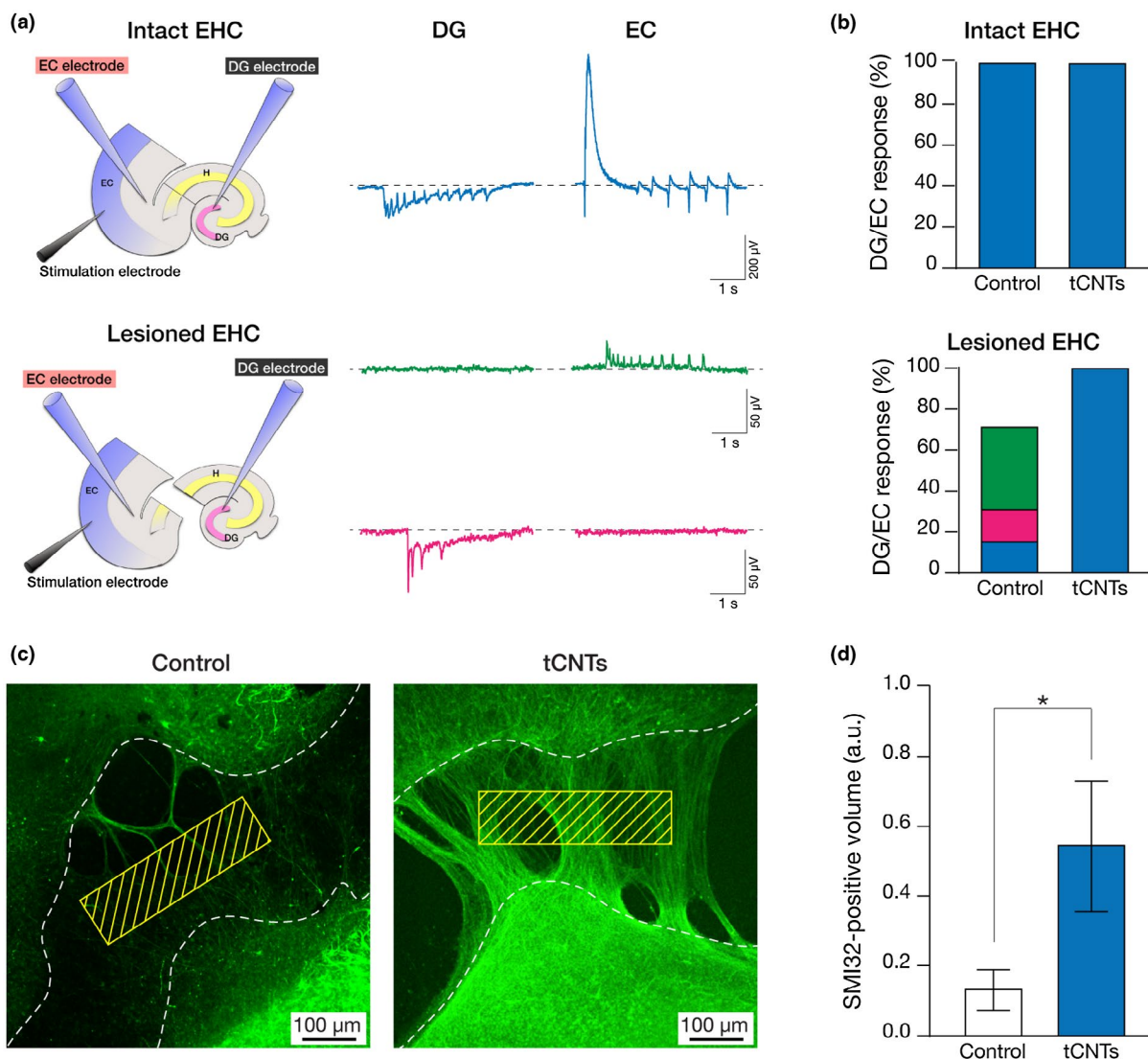

FIGURE 5 tCNTs induce the sprouting of functionally active fibers crossing the lesioned area. (a) A sketch (left) of the experimental configuration used to evaluate EC/DG intercommunication ability through the PP in intact and lesioned EHC using a stimulation electrode inserted into the EC superficial layer. Some representative traces from DG and EC recordings of a lesioned EHC were shown (right). Note the three kind of evoked responses we could observe: simultaneously from both areas (in blue), just from EC (in green), and just from DG (in magenta). (b) Bat plots summarizing the distribution of the three categories of evoked responses in intact (top) and injured (bottom) EHC, both for Controls and tCNTs. (c) Representative confocal images showing the sprouting of SMI32-positive fibers (in green) into the lesioned area. As summarized in the bar plot in (d) cultures grown onto tCNTs displayed a significantly higher percentage of SMI32-positive volume with respect to Controls

in injured EHCs, evoked responses in the two groups diverged. In injured Control organ slices, only in 12.5% of cases PP stimulation evoked a LFP in both EC and DG, while in the majority of case (50%) only EC responses were evoked. Intriguingly, in 12.5% of cases only LFP in DG was evoked, with the remaining 25% of slices unresponsive. Notably, in injured EHCs interfaced to tCNTs, we elicited evoked LFPs from both areas in 100% of cases, as in intact slices (Figure 5b, bottom; Control: $n = 8$; tCNTs: $n = 6$). This evidence further strengthens the hypothesis that the slices recovered a l (re)connection with similar evoked LFPs of the intact (i.e., not lesioned) structure when cultured onto tCNT platforms. Eventually, we investigated if the tCNT-related increase in EC/H synchronized activity and PP stimulation evoked responses were attributable to an increased number of newly generated fibers interconnecting the EC and H sections and able to carry effective electrochemical signals. To address this point, we performed via immunohistochemistry a quantification of SMI32-positive axons (see Methods) crossing the gap separating H and EC (Figure 5c). In injured ECH interfaced to tCNTs, we detected a significantly larger amount of SMI32-positive "crossing-fibers" sprouting into the lesioned area with respect to the Control counterparts (Control: $n = 7$, tCNT: $n = 6$; $p = .02$; Figure 5d). Together with the previous electrophysiological findings, this result shows that tCNTs enhanced the regeneration of axons and their synaptic targeting between EC and DG, re-establishing an active crosstalk between the two separated areas of the sectioned tissue.

3 | DISCUSSION

CNTs have contributed considerably to developments in tissue engineering (Edwards, Werkmeister, & Ramshaw, 2009) and nanomedicine (Erol et al., 2017; Marchesan, Kostarelos, Bianco, & Prato, 2015) due to their unique physical features (O'Connell, 2006) and hold the potential to further contribute to the design of novel nanodevices and neural interfaces (Bareket-Keren & Hanein, 2013; Pancrazio, 2008). In this study, we report a novel CCVD-based approach in CNT synthesis generating uniform carpets of entangled nanotubes on fused silica supporting substrates. Differently from commonly used CVD or drop casting CNT decorating methodologies (Chena, Lib, Linc, Hsud, & Wange, 2012; Lovat et al., 2005; Mazzatenta et al., 2007; Rago et al., 2019) by our new approach we manufactured optically transparent (Anguita et al., 2013) CNT substrates characterized by mechanical stability due to their strong adhesion to the underneath surface. These features made our novel films of tCNTs of particular interest in (neuro)-biology applications where the substrate mechanical stability and the use of techniques demanding

transmission of visible light through the samples are required. Our main results are that tCNT-based substrates when challenged with dissociated and organ CNS cultures were biocompatible, allowing the development of neuronal synaptic networks, and maintained CNT characterizing features of potentiating neural transmission at the interface (Cellot et al., 2011; Lovat et al., 2005; Rago et al., 2019) and promoting axons regrowth (Fabbro et al., 2012; Usmani et al., 2016).

Hippocampal dissociated cultures interfaced to tCNTs were characterized by CNS cell densities and neuron/glia ratios comparable to Controls; the viability of neurons on tCNTs was also supported by the values of the cell passive membrane properties, accepted indicators of neuronal health (Carp, 1992; Gao, Liu, Li, & Wang, 2015). Despite the similarities in network size, tCNTs neurons displayed increased synaptic activity, probably due to the described synaptogenic effects of CNTs, acting as artificial biomimetic clues (Cellot et al., 2011; Pampaloni et al., 2018; Rago et al., 2019).

We scaled up the system by developing organotypic cultures, to investigate the regenerative potentials of tCNTs. Organotypic CNS explants are a well-established technique, such slice cultures maintain a three-dimensional (3D) organization, preserve the cytoarchitecture and cell populations of the organ of origin and provide excellent experimental access to electrophysiology, live imaging, and morphology analyses (Fabbro et al., 2012; Usmani et al., 2016). Accordingly, EHC organ cultures are 3D explants of the CNS in which the overall functional and anatomical neuronal connections are preserved (Del Turco & Deller, 2007; Vlachos et al., 2012). In accordance with our previous studies (Fabbro et al., 2012) interfacing EHCs to tCNTs improved spontaneous network activity and potentiated LFP synchronization. We hypothesize that these effects are ultimately related to an increase in synaptic efficacy due to increased synapse formation at the interface with the large surface, roughness, and conductivity of tCNTs (Fabbro et al., 2012), although we cannot exclude other mechanisms, such as ability of the conductive tCNTs to mediate a direct electrical transmission within the cultured EHC areas.

To address the regenerative ability of tCNTs interfaces, we adopted the perforant patch lesion model, a brain injury model that disrupts the main excitatory input to the DG (Vlachos et al., 2012). Upon a complete transection of the PP, we cultured surgically separated H and EC components to the end of assessing denervation-induced regenerative activity reconnecting the two structures and eventually leading to functional recovery. Indeed in Controls such a procedure leads to a loss of activity in DG and EC structures, indicative of a limited regenerative ability. We did not detect any form of synaptic plasticity, such as homeostatic synaptic scaling, due to denervation (Vlachos et al., 2012). Although we cannot exclude that such changes need single cell recording approaches for being detected, it is also feasible that at the time

of recordings (>1 week after denervation) this transient adaptation to the loss of excitatory drive had returned to baseline values (Vlachos et al., 2012). tCNTs, upon axonal regeneration re-established the appropriate excitatory connections, at least in part, as indicated by evoked LFPs, synchronization of spontaneous LFPs and frequency of LFPs. The latter increase in activity, even higher than in intact structures, might indicate an overall increase in excitability, potentially due to long-lasting plasticity compensation, again sustained by the conductive substrates. In previous studies, we have shown that CNT-based interfaces possess regenerative abilities when interfaced to spinal cord explants (Fabbro et al., 2012; Usmani et al., 2016). In particular, an increased growth cone activity was associated to direct interactions among axons and CNTs, via formation of membrane/material tight junctions (Fabbro et al., 2012). Modulating mechanical forces and adhesion may activate cascades of biochemical signaling relevant to CNS reconstruction.

In conclusion, by introducing a new method to synthesize CNTs and demonstrating for the first time the benefits that this substrate is bringing to lesioned organotypic EHCs cultures, we strengthened the notion of the use of physical features alone to guide different biological responses: tCNTs, with their peculiar transparency coupled to the regenerative effects, stand as a promising material to be exploited in a broad range of applications, from the development of new research tools to the design of devices able to actively interface neural tissue reconstruction.

4 | MATERIALS AND METHODS

4.1 | tCNTs synthesis

MWNTs were synthesized by the decomposition of acetylene (carbon source) catalyzed by iron NPs. NPs were obtained thermally annealing a thin layer of iron evaporated on fused silica (SiO_2) wafer chips, acting as transparent supporting substrates (Ward, Wei, & Ajayan, 2003). Fused silica wafers were manually cleaved into 15×15 mm^2 slices using a diamond scribe and cleaned following the Radio Corporation of America (RCA) method (Kern & Puotinen, 1970). Subsequently, a thin layer of iron (0.2–1 nm in thickness) was deposited directly above the SiO_2 chips surfaces using an electron beam (e-beam) evaporator. Iron film thickness was monitored using an in situ quartz crystal microbalance. Since catalyst layer uniformity plays a crucial role in CNTs synthesis and growth, an average deposition rate of 0.2 Å/s was adopted. The as-evaporated substrates were placed above the heating element of a high-vacuum reaction chamber. An annealing treatment (4 min at $660 \pm 10°C$ in H_2 atmosphere) was performed to: (i) reduce iron oxides resulting from the exposition of the samples to the atmospheric air during the transfer from the e-beam deposition system to the high-vacuum CVD reactor and (ii) to induce the nucleation from the continuous iron layer of homogeneously distributed NPs which will act as nucleation sites for the CNTs growth. Once this treatment process was over, acetylene was introduced in the reaction chamber up to a partial pressure of about 10–20 mbar. Sample temperature was increased to 730°C and reaction time was limited to 90 s, resulting in the formation of a uniform carpet of CNTs of less than 2 μm in thickness. After that, samples were let to cool down to room temperature (RT) and employed as removed from the reaction chamber.

4.2 | tCNTs characterization

Field emission scanning electron microscopy (FE-SEM) imaging was performed on the as-produced CNTs using a Gemini SUPRA 40 SEM (Carl Zeiss NTS GmbH, Oberkochen, Germany) operating at an accelerating voltage of 5 keV. Transmission electron microscopy (TEM) of CNT carpets was performed using an EM 208-Philips TEM system equipped with Quemesa (Olympus Soft Imaging Solutions) camera. Before TEM imaging, samples were released from the substrates, dispersed in ethanol and drop casted onto a commercial lacey carbon TEM grid. Transmission spectra in the visible spectral range (400–700 nm) were acquired with an Agilent Technologies Cary-60 UV–VIS spectrophotometer at a scan speed of 600 nm/min and 1-nm resolution. CCVD CNT film thicknesses were evaluated performing atomic force microscopy (Solver Pro, NT-MDT, RU) across a scratch in the film done with a scalpel and exposing the underneath fused silica substrate. Raman spectroscopy was conducted on the as-produced CNTs at RT employing a Renishaw inVia Raman microscope with a 60× objective lens at 632.8-nm laser excitation and a laser power of about 2 mW. In order to evaluate the CNTs surface composition, X-ray photoelectron spectroscopy (XPS) was carried out on a VG Escalab II spectrometer, in constant pass energy mode. Non-monochromatized Al Kα exciting radiation (1,486.6 eV, 225 W) was used. Core-level XPS data analysis was performed after the removal of nonlinear Shirley background and deconvolution into Gaussian/Lorentzian components using Igor Pro 6.36 software (Wavemetrics Co., US).

4.3 | Ethics

All procedures were approved by the local veterinary authorities and performed in accordance with the Italian law (decree 26/14) and the UE guidelines (2007/526/CE and 2010/63/UE). The animal use was approved by the Italian Ministry of Health. All efforts were made to minimize suffering and to reduce the number of animals used.

4.4 | Primary cultures

Hippocampal neurons were obtained from neonatal Wistar rats (postnatal day: P2–P3) as previously reported (Cellot et al., 2009; Lovat et al., 2005). Briefly, cells were plated either on poly-L-ornithine-coated (Sigma Aldrich; Controls) or on tCNTs-coated glass coverslips and incubated at 37°C, 5% CO_2, in Neurobasal-A (Thermo Fischer) medium containing B27 2% (Gibco), Glutamax 10 mM, and Gentamycin 0.5 μM (Gibco). Cultured neurons were used for experiments at 8–10 DIV.

4.5 | Organotypic cultures

Organotypic slice cultures were prepared according to the roller tube technique, previously described (Gähwiler, 1988; Mohajerani & Cherubini, 2005). Briefly, 400-μm-thick EHCs slices were obtained from P6 to P8-old Wistar rats (the perforant pathway is described to be fully developed in rats from P6; Fricke & Cowan, 1977) by means of a tissue chopper (McIlwan) and stored for 1h in cold (4°C) Gey's Balanced Salt Solution medium (GBSS) enriched with glucose and kynurenic acid to limit excitotoxic processes. The slices were subsequently plated onto glass Control coverslips or tCNTs covered fused silica slices and embedded in chicken plasma (16 μl; SIGMA), which was coagulated with the addition of a drop of thrombin (23 μl). The lesion was made with a scalpel and under microscopy at the subicular level and the EC portion was placed from 400 to 600 μm far from the hippocampus one. This was accomplished taking advantage of a graduated ruler placed below the coverslips during plating. Cultures were then left for 1 hr at RT and then placed in Nunc^{TM} tubes filled with 750 ml of Neurobasal-A (Thermo Fischer) medium containing B27 2% (Gibco), Glutamax 10 mM and Gentamycin 0.5 μM (Gibco). Tubes were incubated at 37°C in a roller drum (0.17 RPM) and used for experiments after 8–12 DIV. The medium was completely replaced every 3 days.

4.6 | Patch-clamp experiments

Patch-clamp, whole-cell recordings were achieved with glass micropipettes with a resistance of 4–7 MΩ. The intracellular pipette solution was the following: 120 mM K-gluconate, 20 mM KCl, 10 mM HEPES, 10 mM EGTA, 2 mM $MgCl_2$, 2 mM Na_2ATP, and pH 7.3. Cultures were positioned in a custom-made chamber mounted on an inverted microscope (Eclipse TE-200, Nikon, Japan) and continuously superfused with external solution at a rate of 5 ml/min. The external saline solution contained: 150 mM NaCl, 4 mM KCl, 1 mM $MgCl_2$, 2 mM $CaCl_2$, 10 mM HEPES, 10 mM glucose, and pH 7.4. Cells were voltage clamped at a holding potential of −56 mV (not corrected for liquid junction potential, that was calculated to be 13.7 mV at 20°C in our experimental conditions). The (uncompensated) series resistance had values lower than 8 MΩ. All recordings were performed at RT. Data were collected using a Multiclamp 700A patch amplifier connected to a PC through a Digidata 1440 (Molecular Devices, US) and subsequently analyzed using Clampfit 10.4 software suite (Molecular Devices, US).

4.7 | Field potential recordings

Simultaneous extracellular field potential recordings from visually identified molecular layer of the DG and the superficial layers of the EC were performed on slices at 8–12 DIV at RT using low resistance (4–6 MΩ) glass micropipettes filled with extracellular solution. For each experiment, the organotypic slices were cultured onto Control glass coverslips and tCNT-decorated fused silica slides, positioned into a recording chamber, mounted onto an upright microscope (Eclipse TE-200, Nikon, Japan) and superfused with standard saline solution containing: 152 mM NaCl, 4 mM KCl, 1 mM $MgCl_2$, 2 mM $CaCl_2$,10 mM HEPES, and 10 mM glucose. The pH was adjusted to 7.4 with NaOH. After a stabilization period of about 20 min, the recordings of the spontaneous activity were sampled for additional 45 min in standard saline solution. Finally, as control of the excitatory nature of the recorded neuronal signals, we evaluated the activity for 15 min in the presence of CNQX (10 μM) and no LFPs were detected. All data were collected using a Multiclamp 700A amplifier connected to a PC through a Digidata 1440 (Molecular Devices, US) and subsequently analyzed using Clampfit 10.4 software suite (Molecular Devices, US). To stimulate the PP we placed a bipolar electrode, made by a low-resistance patch pipette containing normal saline solution, into the EC superficial layers, no changes in the electrode position were made. Voltage pulses (from 200 to 1,000 μs) of increasing amplitude (from 1 to 50 V) were delivered by an isolated voltage stimulator (DS2A; Digitimer ltd.) until a response was evoked and detected. The synchrony between DG and EC LFPs was assessed through a MATLAB custom-made script, as previously described (Usmani et al., 2016). Briefly, for each pair of voltage time series, the Pearson correlation coefficient (CCF) was assessed and its statistical significance was determined by performing a permutation test. This test measures the distribution of correlation coefficients that one would expect to observe if the voltage signals recorded from a pair of explants happened to correlate purely by chance. By measuring how likely it was for the values of this null distribution to be larger or equal than the real correlation coefficient, it was possible to understand whether the correlation between the pair of time series was significantly larger than expected by chance. This procedure allowed for determining what fraction of cocultured slices exhibited a significantly

synchronous LFPs, for all the tested conditions (Aurand et al., 2017; Usmani et al., 2016).

4.8 | Immunocytochemistry and microscopy

To visualized dissociated hippocampal neurons, we fixed cultures in 4% formaldehyde (prepared from fresh paraformaldehyde; Sigma) in PBS for 20 min, permeabilized with 0.3% Triton X-100 and incubated with primary antibodies for 30 min at RT. After washing in PBS, cultures were incubated with secondary antibodies for 45 min and then mounted with Vectashield® (Vector Laboratories) on 1-mm-thick microscope glass slides. To visualize neurons and glial cells, we used the following: rabbit anti-β-Tubulin III primary antibody (Sigma T2200, 1:250 dilution), and Alexa 594 goat anti-rabbit secondary antibody (Thermo-Fisher, 1:500); anti-GFAP mouse primary antibody (SIGMA, 1:250) and Alexa 488-goat anti-mouse secondary antibody (Thermo-Fisher, 1:500). Cell nuclei were visualized with the nuclear marker DAPI (1:1,000). Cultures were imaged with an epifluorescence microscope using 10× and 20× objectives (DM 6000, Leica) and analyzed with the open-source software ImageJ (http://rsb.info.nih.gov/ij/). To stain Organotypic cultures we fixed them for 1h at RT as described above. After PBS washes, cultures were incubated with mouse SMI32 (1:250) and rabbit NeuN (SIGMA; 1:200) primary antibodies, and Alexa 594 goat anti-rabbit (Invitrogen, 1:500), Alexa 488 goat anti-mouse (Invitrogen, 1:500) secondary antibodies and Hoechst (Invitrogen; 1:1,000). Cultures were then mounted with Vectashield® (Vector Laboratories) on 1-mm-thick microscope glass slides, visualized with a confocal microscope (Nikon Eclipse Ti-E; 10× objective) and analyzed with the Volocity image analysis software (Perkin Elmer). To quantify the SMI32-positive "crossing-fibers," we selected 3D region of interest (ROI) (500 μm × 50 μm × 15 μm) in the gap between the H and the HC (with the ROI longitudinal axis perpendicular to the segment connecting the centers of the two EHC emi-sections, see Figure 5c) in both Controls and tCNTs cultures. The amount of SMI32-positive voxel within each ROI was quantified for each image, and normalized to the overall ROI volume. All the image values from the same condition were then averaged together and plotted.

4.9 | Statistics

All reported values are expressed as means ± SD, with n indicating the number of cultures, unless otherwise specified. Statistically significant differences between pairs of data sets were assessed by Student's t-test (after validation of variance homogeneity by Levene's test) for parametric data and by either the Mann–Whitney U test or the Kolmogorov–Smirnov test for nonparametric data. When multiple groups were compared, Kruskal–Wallis test was used. Correlation and IEIs of local field potentials were measured through two different custom programs wrote in MATLAB (The MathWorks, Inc., Natick, Massachusetts, United States) (Usmani et al., 2016). Statistical significance was determined at $p < .05$.

CONFLICT OF INTEREST

The authors declare that they have no competing interests.

AUTHOR CONTRIBUTIONS

D.S., L.B., and A.G. conceived the study and wrote the MS; N.P.P., I.R., and I.C. carried out the experiments and analysis. L.C. contributed to the XPS characterization and analysis.

DATA AVAILABILITY STATEMENT

All data needed to evaluate the conclusions in the paper are present in the paper. Additional data related to this paper may be requested from the authors.

REFERENCES

Anguita, J. V., Cox, D. C., Ahmad, M., Tan, Y. Y., Allam, J., & Silva, S. R. P. (2013). Highly transmissive carbon nanotube forests grown at low substrate temperature. *Advanced Functional Materials*, *23*, 5502–5509. https://doi.org/10.1002/adfm.201300400

Antunes, E. F., Lobo, A. O., Corat, E. J., & Trava-Airoldi, V. J. (2007). Influence of diameter in the Raman spectra of aligned multi-walled carbon nanotubes. *Carbon*, *45*(5), 913–921. https://doi.org/10.1016/j.carbon.2007.01.003

Aurand, E. R., Usmani, S., Medelin, M., Scaini, D., Bosi, S., Rosselli, F., … Ballerini, L. (2017). Nanostructures to engineer 3D neural-interfaces: Directing axonal navigation toward successful bridging of spinal segments. *Advanced Functional Materials*, *28*, 1700550. https://doi.org/10.1002/adfm.201700550

Bareket-Keren, L., & Hanein, Y. (2013). Carbon nanotube-based multi electrode arrays for neuronal interfacing: Progress and prospects. *Frontiers in Neural Circuits*, *9*, 122. https://doi.org/10.3389/fncir.2012.00122

Bayer, B. C., Hofmann, S., Castellarin-Cudia, C., Blume, R., Baehtz, C., Esconjauregui, S., … Robertson, J. (2011). Support−catalyst−gas interactions during carbon nanotube growth on metallic Ta films. *The Journal of Physical Chemistry C*, *115*, 4359–4369. https://doi.org/10.1021/jp102986f

Bulusheva, L. G., Okotrub, A. V., Kinloch, I. A., Asanov, I. P., Kurenya, A. G., Kudashov, A. G., … Song, H.. (2008) Effect of nitrogen doping on Raman spectra of multi-walled carbon nanotubes. *Physica Status Solidi (B) Basic Research*, *245*, 1971–1974.

Carp, J. S. (1992). Physiological properties of primate lumbar motoneurons. *Journal of Neurophysiology*, *68*, 1121–1132. https://doi.org/10.1152/jn.1992.68.4.1121

Cellot, G., Cilia, E., Cipollone, S., Rancic, V., Sucapane, A., Giordani, S., … Ballerini, L. (2009). Carbon nanotubes might improve neuronal performance by favouring electrical shortcuts. *Nature Nanotechnology*, *4*, 126–133. https://doi.org/10.1038/nnano.2008.374

Cellot, G., Toma, F. M., Varley, Z. K., Laishram, J., Villari, A., Quintana, M., … Ballerini, L. (2011). Carbon nanotube scaffolds tune synaptic strength in cultured neural circuits: Novel frontiers in nanomaterial-tissue interactions. *Journal of Neuroscience*, *31*, 12945–12953. https://doi.org/10.1523/JNEUROSCI.1332-11.2011

Cetin, M., Gumru, S., & Aricioglu, F. (2012). Nanotechnology applications in neuroscience: Advances, opportunities and challenges. *Bulletin of Clinical Psychopharmacology*, *22*, 115–120. https://doi.org/10.5455/bcp.20120621044747

Charlier, J. C. (2002). Defects in carbon nanotubes. *Accounts of Chemical Research*, *35*, 1063–1069.

Chena, C., Lib, C., Linc, K., Hsud, T., & Wange, S. (2012). A green process to prepare hydrophobic and transparent CNT-based surface. *Key Engineering Materials*, *521*, 171–178. https://doi.org/10.4028/www.scientific.net/KEM.521.171

Chiang, W.-H., & Sankarana, R. M. (2007). Microplasma synthesis of metal nanoparticles for gas-phase studies of catalyzed carbon nanotube growth. *Applied Physics Letters*, *91*, 121503.

Chiodarelli, N., Richard, O., Bender, H., Heyns, M., De Gendt, S., Groeseneken, G., & Vereecken, P. M. (2012). Correlation between number of walls and diameter in multiwall carbon nanotubes grown by chemical vapor deposition. *Carbon*, *50*, 1748–1752. https://doi.org/10.1016/j.carbon.2011.12.020

Costa, S., Borowiak-Palen, E., Kruszyńska, M., Bachmatiuk, A., & Kaleńczuk, R. J. (2008). Characterization of carbon nanotubes by Raman spectroscopy. *Materials Science-Poland*, *26*, 433–441.

Del Turco, D., & Deller, T. (2007). Organotypic entorhino-hippocampal slice cultures-a tool to study the molecular and cellular regulation of axonal regeneration and collateral sprouting in vitro. *Methods in Molecular Biology*, *399*, 55–66.

Edwards, S. L., Werkmeister, J. A., & Ramshaw, J. A. (2009). Carbon nanotubes in scaffolds for tissue engineering. *Expert Review of Medical Devices*, *6*, 499–505. https://doi.org/10.1586/erd.09.29

Eleftheriou, C. G., Zimmermann, J. B., Kjeldsen, H. D., David-Pur, M., Hanein, Y., & Sernagora, E. (2017). Carbon nanotube electrodes for retinal implants: A study of structural and functional integration over time. *Biomaterials*, *112*, 108–121. https://doi.org/10.1016/j.biomaterials.2016.10.018

Erol, O., Uyan, I., Hatip, M., Yilmaz, C., Tekinay, A. B., & Guler, M. O. (2017). Recent advances in bioactive 1D and 2D carbon nanomaterials for biomedical applications. *Nanomedicine*, *17*, 30089.

Fabbro, A., Villari, A., Laishram, J., Scaini, D., Toma, F. M., Turco, A., … Ballerini, L. (2012). Spinal cord explants use carbon nanotube interfaces to enhance neurite outgrowth and to fortify synaptic inputs. *ACS Nano*, *6*, 2041–2055. https://doi.org/10.1021/nn203519r

Finnie, J. W., & Blumbergs, P. C. (2002). Traumatic Brain Injury. *Veterinary Pathology*, *39*, 679–689. https://doi.org/10.1354/vp.39-6-679

Fricke, R., & Cowan, W. M. (1977). An autoradiographic study of the development of the entorhinal and commissural afferents to the dentate gyrus of the rat. *The Journal of Comparative Neurology*, *173*, 231–250.

Gähwiler, B. H. (1988). Organotypic cultures of neural tissue. *Trends in Neuroscience*, *11*, 484–489. https://doi.org/10.1016/0166-2236(88)90007-0

Gao, Y., Liu, L., Li, Q., & Wang, Y. (2015). Differential alterations in the morphology and electrophysiology of layer II pyramidal cells in the primary visual cortex of a mouse model prenatally exposed to LPS. *Neuroscience Letters*, *591*, 138–143. https://doi.org/10.1016/j.neulet.2015.02.043

Girgis, F., Pace, J., Sweet, J., & Miller, J. P. (2016). Hippocampal neurophysiologic changes after mild traumatic brain injury and potential neuromodulation treatment approaches. *Frontiers in Systems Neuroscience*, *10*, 8.

Guggenmos, D. J., Azin, M., Barbay, S., Mahnken, J. D., Dunham, C., Mohseni, P., & Nudo, R. J. (2013). Restoration of function after brain damage using a neural prosthesis. *Proceedings of the National Academy of Sciences*, *110*, 21177–21182.

Hofmann, S., Blume, R., Wirth, C. T., Cantoro, M., Sharma, R., Ducati, C., … Robertson, J. (2009). State of transition metal catalysts during carbon nanotube growth. *Journal of Physical Chemistry C*, *113*, 1648–1656.

Hokkanen, M., Lautala, S., Flahaut, E., & Ahlskog, M. (2017). Experimental studies on the detachment of multi-walled carbon nanotubes by a mobile liquid interface. *Colloids and Surfaces A: Physicochemical and Engineering Aspects*, *533*, 109–115. https://doi.org/10.1016/j.colsurfa.2017.08.029

Huber, D., Oskooei, A., Casadevall i Solvas, X., DeMello, A., & Kaigala, G. V. (2018). Hydrodynamics in cell studies. *Chemical Reviews*, *118*, 2042–2079.

Iijima, S. (1991). Helical microtubules of graphitic carbon. *Nature*, *354*, 56–58. https://doi.org/10.1038/354056a0

Jacobson, S., & Marcus, E. M. (2008). *Neuroanatomy for the neuroscientist*. New York, NY: Springer.

Kern, W., & Puotinen, D. A. (1970). Cleaning solutions based on hydrogen peroxide for use in silicon semiconductor technology. *RCA Review*, *31*, 187–206.

Kim, K. K., Park, J. S., Kim, S. J., Geng, H. Z., An, K. H., Yang, C. M., … Lee, Y. H. (2007). Dependence of Raman spectra G band intensity on metallicity of single-wall carbon nanotubes. *Physical Review B*, *76*, 205426.

Lee, C. J., Park, J., Huh, Y., & Lee, J. Y. (2001). Temperature effect on the growth of carbon nanotubes using thermal chemical vapor deposition. *Chemical Physics Letters*, *343*, 33–38. https://doi.org/10.1016/S0009-2614(01)00680-7

Lee, J. K., Baac, H., Song, S. H., Jang, E., Lee, S. D., Park, D., & Kim, S. J. (2006). Neural prosthesis in the wake of nanotechnology: Controlled growth of neurons using surface nanostructures. *Acta Neurochirurgica Supplementum*, *99*, 141–144.

Li, D., Field, P. M., Starega, U., Li, Y., & Raisman, G. (1993). Entorhinal axons project to dentate gyrus in organotypic slice co-culture. *Neuroscience*, *52*, 799–813. https://doi.org/10.1016/0306-4522(93)90530-S

Li, D., Field, P. M., Yoshioka, N., & Raisman, G. (1994). Axons regenerate with correct specificity in horizontal slice culture of the postnatal rat entorhino-hippocam system. *European Journal of Neuroscience*, *6*, 1026–1037.

Long, D. A. (1997). *Raman spectroscopy*. London, UK: McGraw-Hill.

Lovat, V., Pantarotto, D., Lagostena, L., Cacciari, B., Grandolfo, M., Righi, M., … Ballerini, L. (2005). Carbon nanotube substrates boost neuronal electrical signaling. *Nano Letters*, *5*, 1107–1110. https://doi.org/10.1021/nl050637m

Maas, A. I., Stocchetti, N., & Bullock, R. (2008). Moderate and severe traumatic brain injury in adults. *The Lancet Neurology*, *7*, 728–741.

Marchesan, S., Kostarelos, K., Bianco, A., & Prato, M. (2015). The winding road for carbon nanotubes in nanomedicine. *Materials Today*, *18*, 12–19. https://doi.org/10.1016/j.mattod.2014.07.009

Mattevi, C., Wirth, C. T., Hofmann, S., Blume, R., Cantoro, M., Ducati, C., … Robertson, J. (2008). In-situ X-ray photoelectron spectroscopy study of catalyst−support interactions and growth of carbon nanotube forests. *Journal of Physical Chemistry C*, *112*, 12207–12213.

Mazzatenta, A., Giugliano, M., Campidelli, S., Gambazzi, L., Businaro, L., Markram, H., … Ballerini, L. (2007). Interfacing neurons with carbon nanotubes: Electrical signal transfer and synaptic stimulation in cultured brain circuits. *Journal of Neuroscience*, *27*, 6931–6936. https://doi.org/10.1523/JNEUROSCI.1051-07.2007

Michaelis, F. B., Weatherup, R. S., Bayer, B. C., Bock, M. C., Sugime, H., Caneva, S., … Hofmann, S. (2014). Co-catalytic absorption layers for controlled laser-induced chemical vapor deposition of carbon nanotubes. *ACS Applied Materials & Interfaces*, *6*, 4025–4032. https://doi.org/10.1021/am405460r

Mohajerani, M. H., & Cherubini, E. (2005). Spontaneous recurrent network activity in organotypic rat hippocampal slices. *European Journal of Neuroscience*, *22*, 107–118.

Morassutto, M., Tiggelaara, R. M., Smithers, M. A., & Gardeniersa, G. E. (2016). Vertically aligned carbon nanotube field emitter arrays with Ohmic base contact to silicon by Fe-catalyzed chemical vapor deposition. *Materials Today Communications*, *7*, 89–100. https://doi.org/10.1016/j.mtcomm.2016.04.007

Mudimela, P. R., Scardamaglia, M., González-León, O., Reckinger, N., Snyders, R., Llobet, E., … Colomer, J. (2014). Gas sensing with gold-decorated vertically aligned carbon nanotubes. *Beilstein Journal of Nanotechnology*, *5*, 910–918.

Nelson, C. (2017). From static to animated: Measuring mechanical forces in tissues. *Journal of Cell Biology*, *216*, 29–30.

O'Connell, M. J. (2006). *Carbon nanotubes: Properties and applications* (1st ed.). CRC Press, Taylor e Francis Group.

Okpalugo, T. I. T., Papakonstantinou, P., Murphy, H., McLaughlin, J. A. D., & Brown, N. M. D. (2005). High resolution XPS characterization of chemical functionalised MWCNTs and SWCNTs. *Carbon*, *43*, 153–161. https://doi.org/10.1016/j.carbon.2004.08.033

Pampaloni, N. P., Scaini, D., Perissinotto, F., Bosi, S., Prato, M., & Ballerini, L. (2018). Sculpting neurotransmission during synaptic development by 2D nanostructured interfaces. *Nanomedicine*, *14*, 2521–2532. https://doi.org/10.1016/j.nano.2017.01.020

Pancrazio, J. J. (2008). Neural interfaces at the nanoscale. *Nanomedicine (London)*, *3*, 823–830. https://doi.org/10.2217/17435889.3.6.823

Parnavelas, J., Lynch, G., Brecha, N., Cotman, C., & Globus, A. (1974). Spine loss and regrowth in hippocampus following deafferentation. *Nature*, *248*, 71–73. https://doi.org/10.1038/248071a0

Perederiy, J. V., Luikart, B. W., Schnell, E., & Westbrook, G. L. (2013). Neural injury alters proliferation and integration of adult-generated neurons in the dentate gyrus. *Journal of Neuroscience*, *33*, 4754–4767.

Perederiy, J. V., & Westbrook, G. L. (2013). Structural plasticity in the dentate gyrus—Revisiting a classic injury model. *Frontiers in Neural Circuits*, *7*, 17. https://doi.org/10.3389/fncir.2013.00017

Perlmutter, J. S., & Mink, J. W. (2006). Deep brain stimulation. *Annual Review of Neuroscience*, *29*, 229–257.

Rago, I., Rauti, R., Bevilacqua, M., Calaresu, I., Pozzato, A., Cibinel, M., … Scaini, D. (2019). Carbon nanotubes, directly grown on supporting surfaces, improve neuronal activity in hippocampal neuronal networks. *Advanced Biosystems*, *3*(5), 1800286–https://doi.org/10.1002/adbi.201800286.

Roeges, N. P. G. (1997). *A guide to the complete interpretation of infrared spectra of organic structures*. Chichester, UK: John Wiley and Sons.

Saito, R., Grüneis, A., Samsonidze, G. G., Brar, V. W., Dresselhaus, G., Dresselhaus, M. S., … Filho, A. G. S. (2003). Double resonance Raman spectroscopy of single-wall carbon nanotubes. *New Journal of Physics*, *5*, 157.

Shah, K. A., & Tali, B. A. (2016). Synthesis of carbon nanotubes by catalytic chemical vapour deposition: A review on carbon sources, catalysts and substrates. *Materials Science in Semiconductor Processing*, *41*, 67–82. https://doi.org/10.1016/j.mssp.2015.08.013

Steward, O., & Vinsant, S. L. (1983). The process of reinnervation in the dentate gyrus of the adult rat: A quantitative electron microscopic analysis of terminal proliferation and reactive synaptogenesis. *Journal of Comparative Neurology*, *214*, 370–386.

Tscherter, A., Heuschkel, M., Renaud, P., & Streit, J. (2001). Spatiotemporal characterization of rhythmic activity in rat spinal cord slice cultures. *European Journal of Neuroscience*, *14*, 179–190.

Usmani, S., Aurand, E. R., Medelin, M., Fabbro, A., Scaini, D., Laishram, J., … Ballerini, L. (2016). 3D meshes of carbon nanotubes guide functional reconnection of segregated spinal explants. *Science Advances*, *2*, e1600087. https://doi.org/10.1126/sciadv.1600087

Vidu, R., Rahman, M., Mahmoudi, M., Enachescu, M., Poteca, T. D., & Opris, I. (2014). Nanostructures: A platform for brain repair and augmentation. *Frontiers in Systems Neuroscience*, *8*, 91.

Vitale, F., Summerson, S. R., Aazhang, B., Kemere, C., & Pasquali, M. (2015). Neural stimulation and recording with bidirectional, soft carbon nanotube fiber microelectrodes. *ACS Nano*, *9*, 4465–4474. https://doi.org/10.1021/acsnano.5b01060

Vlachos, A., Becker, D., Jedlicka, P., Winkels, R., Roeper, J., & Deller, T. (2012). Entorhinal denervation induces homeostatic synaptic scaling of excitatory postsynapses of dentate granule cells in mouse organotypic slice cultures. *PLoS ONE*, *7*, e32883. https://doi.org/10.1371/journal.pone.0032883

Vuksic, M., Del Turco, D., Vlachos, A., Schuldt, G., Müller, C. M., Schneider, G., & Deller, T. (2011). Unilateral entorhinal denervation leads to long-lasting dendritic alterations of mouse hippocampal granule cells. *Experimental Neurology*, *230*, 176–185.

Wang, M., Mi, G., Shi, D., Bassous, N., Hickey, D., & Webster, T. J. (2017). Nanotechnology and nanomaterials for improving neural interfaces. *Advanced Functional Materials*, *28*, 1700905.

Ward, J. W., Wei, B. Q., & Ajayan, P. M. (2003). Substrate effects on the growth of carbon nanotubes by thermal decomposition of methane. *Chemical Physics Letters.*, *376*, 717–725.

Witter, M. P. (2007). The perforant path: Projections from the entorhinal cortex to the dentate gyrus. *Progress in Brain Research*, *163*, 43–61.

Witter, M. P., & Amaral, D. G. (2004). Hippocampal formation. In G. Paxinos (Ed.), *The rat nervous system* (3rd ed., Vol. *3*, pp. 511–573). Amsterdam, The Netherlands: Elsevier.

Woodhams, P. L., & Atkinson, D. J. (1996). Regeneration of entorhino-dentate projections in organotypic slice cultures: Mode of axonal regrowth and effects of growth factors. *Experimental Neurology*, *140*, 68–78. https://doi.org/10.1006/exnr.1996.0116

Woodhams, P. L., Atkinson, D. J., & Raisman, G. (1993). Rapid decline in the ability of entorhinal axons to innervate the dentate gyrus with increasing time in organotypic co-culture. *European Journal of Neuroscience*, *5*, 1596–1609. https://doi.org/10.1111/j.1460-9568.1993.tb00229.x

Zhang, L., Li, Z., Tan, Y., Lolli, G., Sakulchaicharoen, N., Requejo, F. G., … Resasco, E. D. (2006). Influence of a top crust of entangled nanotubes on the structure of vertically aligned forests of single-walled carbon nanotubes. *Chemistry of Materials*, *18*, 5624–5629. https://doi.org/10.1021/cm061783b